Science Advances

AAAS

advances.sciencemag.org/cgi/content/full/1/10/e1501015/DC1

Supplementary Materials for

Quantum entanglement at ambient conditions in a macroscopic solid-state spin ensemble

Paul V. Klimov, Abram L. Falk, David J. Christle, Viatcheslav V. Dobrovitski, David D. Awschalom

Published 20 November 2015, *Sci. Adv.* **1**, e1501015 (2015)
DOI: 10.1126/sciadv.1501015

The PDF file includes:

Supplementary Materials

§ S1. Multinuclear spin registers

Each R1 and R2 register contains a single PL6 electron spin strongly coupled to a single ^{29}Si nuclear spin. The lattice sites occupied by ^{29}Si atoms to form R1 and R2 registers (sites '1' and '2', respectively) have a non-zero crystal degeneracy. It is therefore possible to have larger spin registers that consist of a single PL6 electron spin strongly coupled to multiple ^{29}Si spins (e.g. R11 has two ^{29}Si atoms at the 1 lattice site, and R112, which has two ^{29}Si atoms at the 1 lattice site and one ^{29}Si atom at a 2 lattice site). These registers occur probabilistically according to the product of binomial distributions (*B)*:

$$B(n_1, k_1, p) * B(n_2, k_2, p) = \binom{n_1}{k_1}\binom{n_2}{k_2} p^{k_1+k_2}(1-p)^{n_1+n_2-k_1-k_2}, \quad \text{(S1)}$$

where the subscripts denote the two lattice sites, n_i is the crystal degeneracy of the ith lattice site and k is the number of those degenerate sites that are occupied by a ^{29}Si atom, which occur in our samples naturally with probability p=4.7%. The crystal degeneracies of R1 and R2 are n_1=3 and n_2=6. These assignments were made in a previous work (*16*) by comparing the intensities of the registers' hyperfine-split ODMR resonances (purple and blue traces in Fig. 2B, for R1 and R2, respectively) to the intensity of the non-hyperfine split ODMR resonance (black trace in Fig. 2B). This assignment is supported by drawing correspondence to similar registers based on SiC divacancies (*16*, *17*, *27*). In particular, the SiC divacancies have registers with nearly identical hyperfine coupling strengths and relative ODMR intensities to R1 and R2, but with known three-fold and six-fold degeneracies.

These multinuclear registers have ODNMR resonances that are approximately degenerate with the R1 and R2 ODNMR resonances, and therefore contribute parasitic signal that interferes with our tomographic reconstructions. Here, we will compute the ratio of this parasitic signal to the R1 and R2 signals to show that it has little impact on our results.

The electron spin resonances (ESR) of registers containing a single PL6 electron spin strongly coupled to up to three ^{29}Si nuclear spins are given in Table S1. We also present these registers' frequency detunings (Δ) from our quantum gates, which depend on whether or not we are performing an experiment on R1 or R2 (labeled "R2 experiment" and "R1 experiment" in Table S1). The maximum signal that a multinuclear register can contribute is reduced by the off-resonant driving factor

$$\frac{\Omega^2}{\Omega^2+\Delta^2}, \tag{S2}$$

where Ω is the drive-field strength. Combining this factor with Eq. (S1), we find that the ratio of signal that comes from unrelated registers to the real signal from R1, for example, is:

$$\frac{\binom{6}{k_1}\binom{3}{k_2}p^{k_1+k_2}(1-p)^{9-k_1-k_2}}{\binom{6}{1}\binom{3}{0}p(1-p)^8}\frac{\Omega^2}{\Omega^2+\Delta^2}. \tag{S3}$$

We compute this quantity in Table S1 (labeled "Relative Signal"), assuming that nuclear spins in all registers optically initialize into the nuclear $\uparrow$ state, which is true for R1 and R2. Summing Eq. (S3) for registers up to those containing 3 nuclear spins and a single electron spin, we see that the parasitic signal is at most ~11% in R1 experiments and ~7% in R2 experiments. We therefore conclude that multinuclear registers contribute only marginally to our signal.

§ S2. Electron spin polarization

The quantum-state tomography in this work relies on differential photoluminescence (PL) measurements between states related by unitary quantum gates. Since unitary operations cannot probe any element of a system's density matrix that is proportional to the identity matrix, the quantum circuits themselves (Fig. 3B-D) are not sufficient to probe a systems absolute density matrix (i.e. one that includes the identity element). Measuring the absolute density matrix is crucial to proving that our system exhibits genuine, as opposed to pseudo, entanglement. As we show in § S5, it suffices to measure the electron spin polarization to reconstruct the absolute density matrix of the initial and all other states. In this section, we describe how we measure the degree of electron polarization of the

optically initialized PL6 defects. The basic principle underlying our measurement is that the radiative lifetimes of PL6's m_S=0 and m_S=-1 spin states are different. Therefore, by optically exciting PL6 defects with a pulsed laser and measuring the relative coefficients of the bi-exponential PL decay, we have a direct measurement of the ground state electron spin polarization.

Since the PL6 defect has been measured (*33*) to have the same C_{3V} symmetry as the nitrogen-vacancy (NV) center in diamond, we adopt the same model and experimental techniques that were used to determine the electron spin polarization of NV centers (*36, 43, 44*). In this model, a color center spin in its optically excited state can, in addition to radiatively decaying in a spin-conserving way, undergo a spin-selective non-radiative intersystem crossing to a singlet state. This transition being spin-dependent, means that the probability of entering the non-radiative intersystem crossing is higher for the $m_S = \pm 1$ spin sublevels than for the $m_S = 0$ spin sublevel. This process enables magnetic transitions between these spin states to be detected through optically detected magnetic resonance (ODMR). Moreover, because the singlet eventually relaxes by undergoing an additional intersystem crossing to the spin triplet *ground* state, repeated cycling of the defect through this transition also polarizes the spin state in its orbital ground state.

In this model, the PL emitted after excitation with a short laser pulse follows a bi-exponential distribution, where the observed lifetimes, τ_0 and $\tau_{\pm 1}$, are the lifetimes for the $m_S = 0$ and $m_S = \pm 1$ spin sublevels, respectively. The lifetimes follow the relation $\tau_i = (\frac{1}{\tau_{optical}} + k_i)^{-1}$, where $\tau_{optical}$ is the bare optical lifetime and k_i is the intersystem crossing rate of the i^{th} spin sublevel. The respective relative amplitudes of the exponentials, then, correspond to the relative occupation of the $m_S = 0$ and $m_S = \pm 1$ spin sublevels in the ground state. Thus, fitting the observed time-correlated single photon counting data to a bi-exponential model allows us to infer the absolute ground state electron spin polarization after non-resonant optical pumping.

To measure the bi-exponential decay, we use a photon counting module (Picoquant PicoHarp 300) to time-resolve the PL emitted from an ensemble of PL6 defects subject to a train of picosecond pulses

of 850 nm light from a mode-locked Ti:Sapphire laser (Coherent Mira 900). We use an electro-optic modulator (Conoptics 350) to pick the pulses down to a repetition rate of approximately four microseconds. We pass these pulses through a fiber (OZ Optics, QMMJ-33-UVVIS-10/125-3A-20), which lengthens the ~200 fs pulses to approximately ~ 1 ps. These pulses are then guided to excite the defects and their emitted PL is collected using a 50 micron core diameter multimode fiber (ThorLabs GIF50). The fiber is coupled into a 150 mm monochromator (Acton 2150i), which is used for spectral filtering with a 1 nm bandwidth, easily isolating the zero phonon line of PL6 (near 1,038 nm) from other sharp spectral features. We couple the output of the monochromator into a single mode fiber (Corning SMF-28e+) that is connected to a closed-cycle superconducting nanowire single photon detector (SingleQuantum, EOS), which has a quantum efficiency of about 28% at this wavelength and a manufacturer-specified timing jitter of ~50 ps.

Because the PL6 zero phonon line sharpens at low temperatures, we cool the sample to T = 20 K (Janis ST500) to increase our photon collection efficiency and relative rejection of luminescence from other sources in the substrate. We collect separate time-correlated photon traces with the monochromator wavelength set to either the PL6 zero-phonon line or two nanometers shorter than the zero-phonon line. We then subtract these data to remove the constant luminescence background and any remaining non-PL6 response. Since the ODMR signal of PL6 defects does not change significantly from 20 K to 296 K (see Supplementary Figure S4 in ref. *(30)*), we assume that the electron-spin polarization is constant over this temperature range. For comparison, the polarization of NV centers in diamond has been measured to remain constant from 2 K to at least 650 K (*36, 44, 45*).

We repeat the experiment with and without the application of 160 ns π-rotations between picosecond pulses (Fig. S1A). Because a single picosecond pulse is likely not enough to completely reinitialize the spins within the optical interrogation volume, the repeated effect of partial repolarization and microwave rotation puts the system into a mixed state. This mixed state need not be a specific mixture, but rather only be different from the no-microwave case. We can then estimate the lifetimes

and polarizations with the parameter estimation technique that we employ. The normalized data from the two cases of the experiment demonstrate clearly by inspection that microwave-induced rotations of the ground state spin do indeed modulate the time trace of the PL decay (Fig. S1B). Since our aim is to infer the polarization when no microwaves are applied, it may not be immediately clear why we choose to repeat the experiment with microwave rotations between excitations pulses. The higher the degree of polarization efficiency in the PL6 optical cycle, the smaller the amplitude of the shorter lifetime decay associated with the $m_s = \pm 1$ spin state will be – in the limit of 100% polarization, this amplitude vanishes and *a priori* estimation of the shorter lifetime and its associated amplitude becomes impossible because the decay is purely mono-exponential. Performing both experiments and then employing a parameter estimation technique that fits both datasets simultaneously and shares the inferred lifetimes between datasets while allowing the amplitudes to remain independent, solves this issue.

To analyze the data, we model the PL observed by following the equation

$$f_{j,k}(t_{j,k}) = A_k \exp\left(-\frac{t_{j,k}}{\tau_{m_s=0}}\right) + B_k \exp\left(-\frac{t_{j,k}}{\tau_{m_s=\pm 1}}\right) + C_k \,, \tag{S4}$$

where $t_{j,k}$ is the time delay of the j^{th} time bin in the k^{th} dataset, and A_k, B_k, and C_k are the amplitudes of the biexponential decays and constant background offset in the k^{th} dataset. Because fitting bi-exponential models and obtaining uncertainties is a difficult problem in a typical least-squares setting, we apply a Bayesian approach to estimating the model parameters (*46*, *47*). In our approach, the exponential decay lifetimes are shared globally but the amplitudes are allowed to vary between datasets using different microwave conditions. We approximate the error as normally distributed with standard deviation $\sigma_{ij} = \eta\sqrt{d_{k,1038\,nm}(t_j) + d_{k,1036\,nm}(t_j)}$, where the d_k's are the photons counted within the same time bin but when the monochromator is collecting on versus off the zero photon line of PL6, and η is a scaling parameter near unity that can account for any noise unexplained by the random error alone. The square root term is simply combining the estimators for the Poisson error of the time bin in each histogram in quadrature for a normal approximation of the Skellam-distributed error of our

subtracted data -- this is a good approximation since for both histograms, the number of counts in each bin always exceeds about 30. Since the bi-exponential model is fit to the subtracted data, the constant offsets C_k are nearly zero. As an aside, the value of η we infer is not significantly different from unity, indicating any systematic errors are likely below the random noise level.

Parameter uncertainties from the marginal posterior probability distributions of Bayesian models are often difficult or impossible to determine analytically, so most practitioners apply numerical techniques based on Markov-Chain Monte Carlo (MCMC) algorithms. These algorithms generate a random walk subject to the condition of detailed balance whose accept/reject probabilities are set by the posterior probability distribution. In this scenario, the random walk converges to its stationary distribution that is exactly the posterior probability distribution. Here we apply MT-DREAM(ZS), a MCMC algorithm that uses sampling from past random walk states and multiple-try Metropolis steps to quickly converge to the posterior probability distribution, even in problems with high-dimension (*47*).

Our computation of the posterior probability distribution reveals the lifetimes $\tau_0 = (13.9 \pm 0.6)$ ns and $\tau_{\pm 1} = (5.4 \pm 1.6)$ ns, where the error bars are 95% credible intervals, and the independent decay amplitudes A_k and B_k for both datasets. The two-dimensional marginal posterior probability distribution for the lifetime parameters shows a disc-shaped peak, indicating good resolution of both lifetimes and low correlation between them in the parameter estimation problem (Fig. S1B, inset). Although the data in Fig. S1B show some obvious difference between the two PL traces by eye, the model-based inference now lets us infer the relative amplitudes of the two decay terms quantitatively.

The relative $m_s = \pm 1$ decay amplitude, $B_k/(A_k + B_k)$, shows the fraction in this state when microwaves are applied unambiguously differs from the no-microwave case, as desired (Fig. S1C). Of particular interest is the $m_s = \pm 1$ component when no microwaves are applied, and our analysis indicates it is not significantly different, in a statistical sense, from zero. This explains why the τ_0 lifetime we infer is in precise agreement with a previous report that used only a mono-exponential decay model of (14 ± 3) ns (*33*). It is indicative of a very high electron spin polarization for this defect under optical

excitation, which we can quantify by the relation $P_k = (A_k - B_k)/(A_k + B_k)$ (Fig. S1C, inset). We therefore determine the optically induced spin polarization with no applied microwaves (P_0) is $93^{+7}_{-13}\%$ with 95% probability. This is the first report of both spin-modulated bi-exponential decay of the PL6 defect and the spin polarization efficiency of its optical cycle, the latter of which enables us to normalize our tomographic data as described in § S5 by direct substitution of values sampled from the marginal posterior of P_0. This means the final fidelities and PPT test values we compute account for uncertainties in both the tomographic reconstructions and the uncertainty in their normalization that derives from uncertainty in P_0.

§ S3. Register-density calculation

The hyperfine coupling constants, the optical transition energy, the optical lifetime, and microwave zero-field-splitting of PL6 are all similar to those of the neutral divacancies in 4H- and 6H-SiC (*16, 17, 27-28, 30, 32-34, 48*). This suggests that PL6 is a perturbation to the divacancy. We use this analogy and optical spectroscopy to estimate the PL6 spin density. In particular, we compare the intensity of the PL6 zero-phonon-line emission to the intensity of the divacancy zero-phonon-line emission in highly implanted SiC samples (where the concentration is high enough to be accurately measured with double-electron-electron-resonance experiments). From this procedure we estimate that the areal density of PL6 defects is $2\text{x}10^{10}$ cm^{-2}. The number of R1 and R2 registers in the optical illumination area is found by combining this density with the natural abundance of ^{29}Si isotopic defects (4.7 %), the number of degenerate crystal lattice sites (3 for R1 and 6 for R2), and the laser spot size (~3 μm in diameter). From this calculation we estimate that there are 10^3 R1 and R2 registers in our optical interrogation volume.

§ S4. Coherent nuclear spin control

We combine register-specific addressability with different radiofrequency pulse sequences to drive nuclear Rabi oscillations (Fig. S2A), to characterize the inhomogeneous nuclear spin-coherence times

(T^*_{2n}) via Ramsey interferometry (Fig. S2B) and to put a lower bound on the homogeneous nuclear spin coherence time via the Hahn-echo sequence (T_{2n}. See Fig. S3C).

Nuclear Rabi oscillations demonstrate the coherent control of ^{29}Si nuclear spins in R1 and R2 registers. The oscillations of R1 do not exhibit beating after many oscillations, which suggests that the R1 hyperfine tensor is highly isotropic. The oscillations of R2 exhibit beating between three closely spaced frequencies (note that this is consistent with the 6-fold degeneracy assigned earlier), which suggests that the R2 hyperfine tensor is anisotropic. However, the ratio of the slowest to the fastest oscillation frequencies is 0.91, which indicates that the anisotropy is small. This is expected given the highly isotropic hyperfine tensors of similar registers based on the divacancies (*27*).

The inhomogeneous nuclear spin coherence time ($T^*_{2n,\,R1} = 29 \pm 2\ \mu$s, $T^*_{2n,\,R2} = 47 \pm 6\ \mu$s) is found to be two orders of magnitude longer than the inhomogeneous electron spin coherence time ($T^*_{2e} \sim 300$ ns). The homogeneous nuclear spin coherence time ($T_{2n,\,R1} = 247 \pm 100\ \mu$s, $T_{2n,\,R2} = 209 \pm 42\ \mu$s) exceeds the homogeneous electron spin coherence time ($T_{2e} \sim 60$ µs at $T = 296$ K), but is surprisingly short. We attribute this to the electronic spin-lattice relaxation (which occurs on timescales $T_{1e} \sim 200\ \mu$s at $T = 296$ K (*28*)), which randomizes the electron spin and limits our measurement. The nuclear spin coherence is likely significantly longer and should be recoverable via selective re-initialization of the electron spin with a short optical pulse.

§ S5. Quantum State Tomography

Register initialization and readout are achieved through optical pumping and PL measurements, respectively. The PL signal is proportional to the intensity of the readout laser in the interrogation volume. Thus, in our measurements, we study the density matrix of registers as averaged over the illumination volume, which is given by the relation $\rho = \frac{\sum_j I(r_j)\rho_j}{\sum_j I(r_j)}$, where r_j is the location of the j-th register, $I(r_j)$ is the laser intensity at the location of this register, and ρ_j is the 2-spin (electron and nuclear spin) density matrix of the register.

In this section we explicitly outline how we measure the elements of ρ. We employ a simplified notation for the register states: $|1\rangle=|0,\uparrow\rangle$, $|2\rangle=|0,\downarrow\rangle$, $|3\rangle=|-1,\uparrow\rangle$, $|4\rangle=|-1,\downarrow\rangle$, $|5\rangle=|+1,\uparrow\rangle$, and $|6\rangle=|+1,\downarrow\rangle$. The PL emitted by PL6 corresponds to the spin occupation probability of each energy eigenstate (ρ_{ii}, where i ranges from 1-6) multiplied by the PL signal that would be obtained if all spins were in that state (K_i). Mathematically, this can be represented as $\sum_{i=1}^{6} K_i \rho_{ii}$.

To reconstruct ρ of a register ensemble, we use the following algorithm: we prepare the register ensemble into its to-be-measured state, operate on it with a sequence of microwave and radiofrequency pulses (represented by the unitary operator U_1), and then measure the PL. We then re-prepare the state, operate on it with a different sequence of microwave and radiofrequency pulses (U_2) and then measure the PL again. The difference between these PL measurements is the signal (see main text Fig. 3B for the circuit-representation of this measurement sequence):

$$Signal = \sum_{i=1}^{6} K_i[(U_1 \rho U_1^t)_{ii} - (U_2 \rho U_2^t)_{ii}]. \quad \text{(S5)}$$

To extract most elements of ρ it suffices to make U_1 and U_2 be a single electron spin rotation followed by a single nuclear spin rotation. By choosing U_1 and U_2 in this way, we also mitigate errors during the tomography procedure. In particular, such pulse sequences start by transferring the to-be-measured density matrix element with a fast electronic pulse onto the highly coherent nuclear spin. Once transferred, nuclear gates and optical pulses are used to probe the element with minimal dephasing. The same considerations were applied in the construction of our entangling algorithm.

Before explicitly defining U_1 and U_2 we introduce an abbreviated notation for the four spin transitions in our system. We define $e0$ to be the local broadband electronic transition of both $|1\rangle\leftrightarrow|3\rangle$ and $|2\rangle\leftrightarrow|4\rangle$, e1 to be the selective non-local electronic transition $|1\rangle\leftrightarrow|3\rangle$, e2 to be the selective non-local electronic transition $|2\rangle\leftrightarrow|4\rangle$, and n to be the selective non-local nuclear transition $|3\rangle\leftrightarrow|4\rangle$. With this notation, U can be conveniently represented as:

$$U_i = R^n_{\phi n}(\theta_n) R^e_{\phi e}(\theta_e), \tag{S6}$$

where the rotation angles θ_e and θ_n, and phases ϕ_e and ϕ_n depend on the measurement sequence. The superscript n is the single nuclear transition that we drive, and the superscript e is one of the above-defined electronic transitions. We make the electron spin rotation be the same for both U_1 and U_2 and vary the phase and the duration of the nuclear spin rotation. By choosing U_1 and U_2 in this way, the contribution to the signal (Eq. (S5)) from the electron spin vanishes, and therefore, we measure only the nuclear-spin contribution (i.e. the measurement uses ODNMR). Moreover, the signal vanishes for all registers without an ODNMR resonance at the nuclear pulse frequency. Since the nuclear pulse bandwidths are significantly narrower than the separation between the R1 and R2 ODNMR resonances, there is virtually no cross talk between these registers. The explicit rotations to determine the coherences and populations are given in Table S2 and S3, respectively, and are also presented in the main text Fig. 3C and D.

The only elements of ρ that cannot be measured by picking U_i as in Eq. (S6) are ρ_{13}, ρ_{24}. To measure these we modify U_i to have another nuclear spin rotation (denoted by primes):

$$U_i = R^n_{\phi n}(\theta_n) R^e_{\phi e}(\theta_e) R'^n_{\phi' n}(\theta'_n). \tag{S7}$$

Since the PL6 electron spin inhomogeneous coherence time T^*_{2e} is shorter than the time it takes to perform the nuclear spin rotation $R'^n_{\phi' n}(\theta'_n)$, such a measurement would be highly inaccurate. We therefore do not measure ρ_{13} or ρ_{24} but rather add an uncertainty to them equal to the maxima allowed by their corresponding diagonal density matrix elements (for example, the uncertainty in ρ_{13} is $\sqrt{\rho_{11}\rho_{33}}$).

To determine the normalization $(K_3 - K_4)$ for all density matrix elements and the optically initialized density matrix, we need seven linearly independent equations. Three equations come from the pulse sequences presented in Table S3 (the fourth is a linear combination of the others). The fourth equation comes from the normalization condition:

$$tr(\rho) = 1, \tag{S8}$$

The fifth and sixth equations come from the symmetry condition that there is equal electron spin polarization into m_s=±1:

$$\rho_{33} = \rho_{55} \; and \; \rho_{44} = \rho_{66}, \tag{S9}$$

The seventh equation comes from our measure of the electron spin polarization (as discussed in § S2):

$$P_e = \rho_{11} + \rho_{22} - \rho_{33} - \rho_{44} - \rho_{55} - \rho_{66} \tag{S10}$$

To compute all other density matrices, we drop the assumptions of Eq. (S9) and (S10), which are valid for only the initialized state, and assume that the spin populations in the m_S=+1 manifold remain constant under all operations within the m_S=0 and m_S=-1 manifolds:

$$\rho_{55} = \rho_{55}^{initial} \; and \; \rho_{66} = \rho_{66}^{initial}. \tag{S11}$$

Eq. (S11) is valid since our microwave pulses, which have a maximum drive strength of 25 MHz and never exceed a 50 MHz bandwidth, are detuned from the transitions $|1\rangle \leftrightarrow |5\rangle$ and $|2\rangle \leftrightarrow |6\rangle$ by approximately 1.6 GHz. There is no redistribution between states $|5\rangle$ and $|6\rangle$ since our radiofrequency pulses, which have a maximum drive strength of 83 kHz and never exceed a 300 kHz bandwidth, are detuned from the $|5\rangle \leftrightarrow |6\rangle$ transition by approximately 560 kHz. Re-thermalization over the duration of the entangling gate (~5 μs long) is negligible.

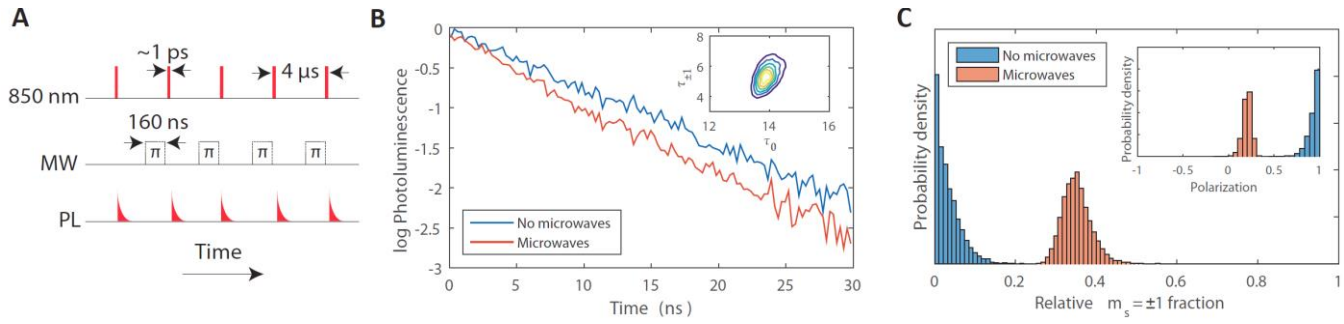

Fig. S1. Optically pumped electron spin polarization. (**A**) A pulse sequence diagram showing the timing of the picosecond pulsed excitation, the microwave (MW) $\boldsymbol{\pi}$-pulses for the case of the experiment where we apply them, and the bi-exponential fluorescence decay recorded on the time-correlated photon counting module. (**B**) The natural logarithm of the normalized binned PL counts from the PL6 ensemble after picosecond pulse excitation for the no-microwave/microwave repetitions of the experiment. Inset: A contour plot of the marginal posterior probability density for the bi-exponential model lifetimes. (**C**) A plot of the marginal probability density of the relative amplitude of the $\boldsymbol{m_s = \pm 1}$ exponential decay term for both the no-microwave/microwave repetitions of the experiment. Inset: The marginal probability density for the spin polarization $\boldsymbol{P_k}$ for the same no-microwave/microwave repetitions of the experiment.

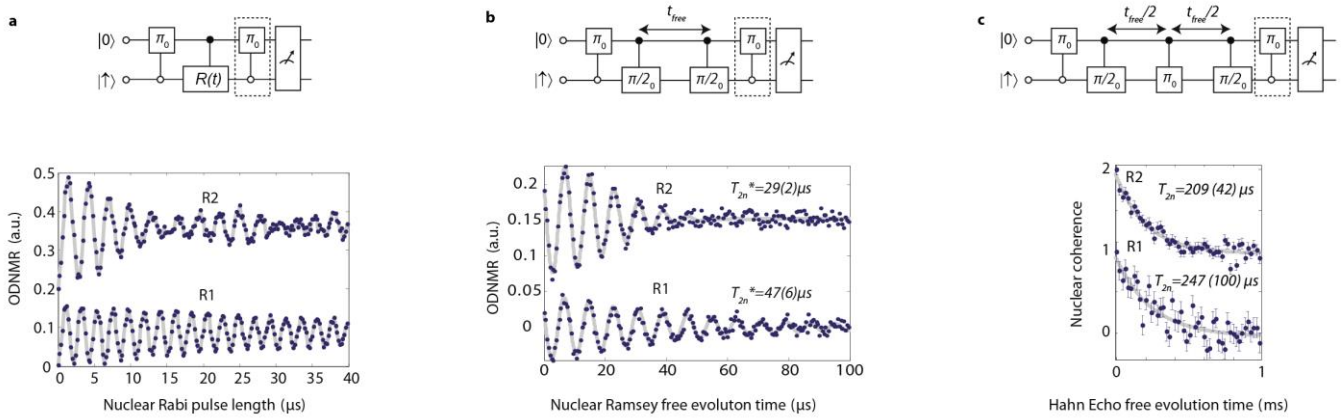

Fig. S2. Coherent nuclear spin control in SiC. (**A**) Nuclear Rabi oscillations. *R*(t) is the variable-length radiofrequency pulse that is used to drive nuclear magnetic resonance. (**B**) Nuclear Ramsey interferometry is used to measure the inhomogeneous nuclear spin coherence time (T^*_{2n}). t_{free} is the nuclear-spin free evolution time. The radiofrequency pulses are applied 125 kHz off resonance to recover an oscillation. (**C**) Nuclear Hahn echo, used to measure the homogeneous nuclear spin coherence time (T_{2n}). t_{free} is the nuclear-spin free evolution time. These measurements were performed at $B_{\|}$=33 mT, where registers initialize into the state $|\mathbf{0},\uparrow\rangle$. The error bars in **(C)** represent 95% confidence intervals. The $C_{\uparrow}NOT_e$ gate in the dashed boxes in the circuit diagrams can be used to project the nuclear spin onto the electron spin for readout. This gate is not necessary near $B_{\|}$=33 mT, where the nuclear spin can be measured directly. The curves in all three panels have been offset for clarity. See the Materials and Methods for measurement details.

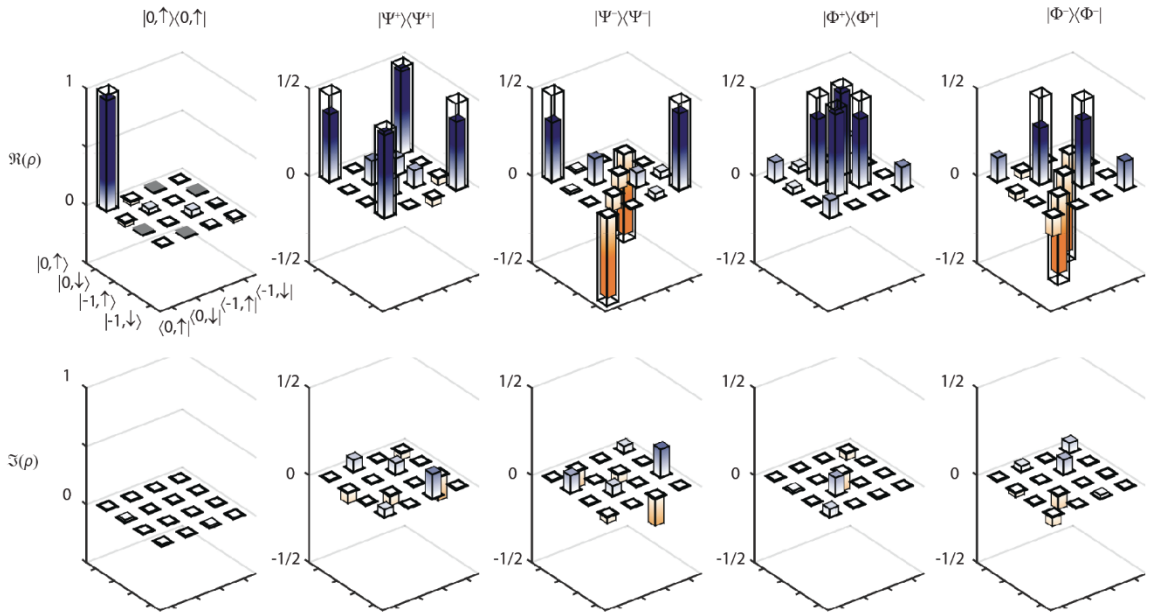

Fig. S3. Entanglement of the R1 ensemble. Real (upper panels) and imaginary (lower panels) components of the initial and entangled R1 density matrices. The overlaid transparent bars represent the ideal density matrices.

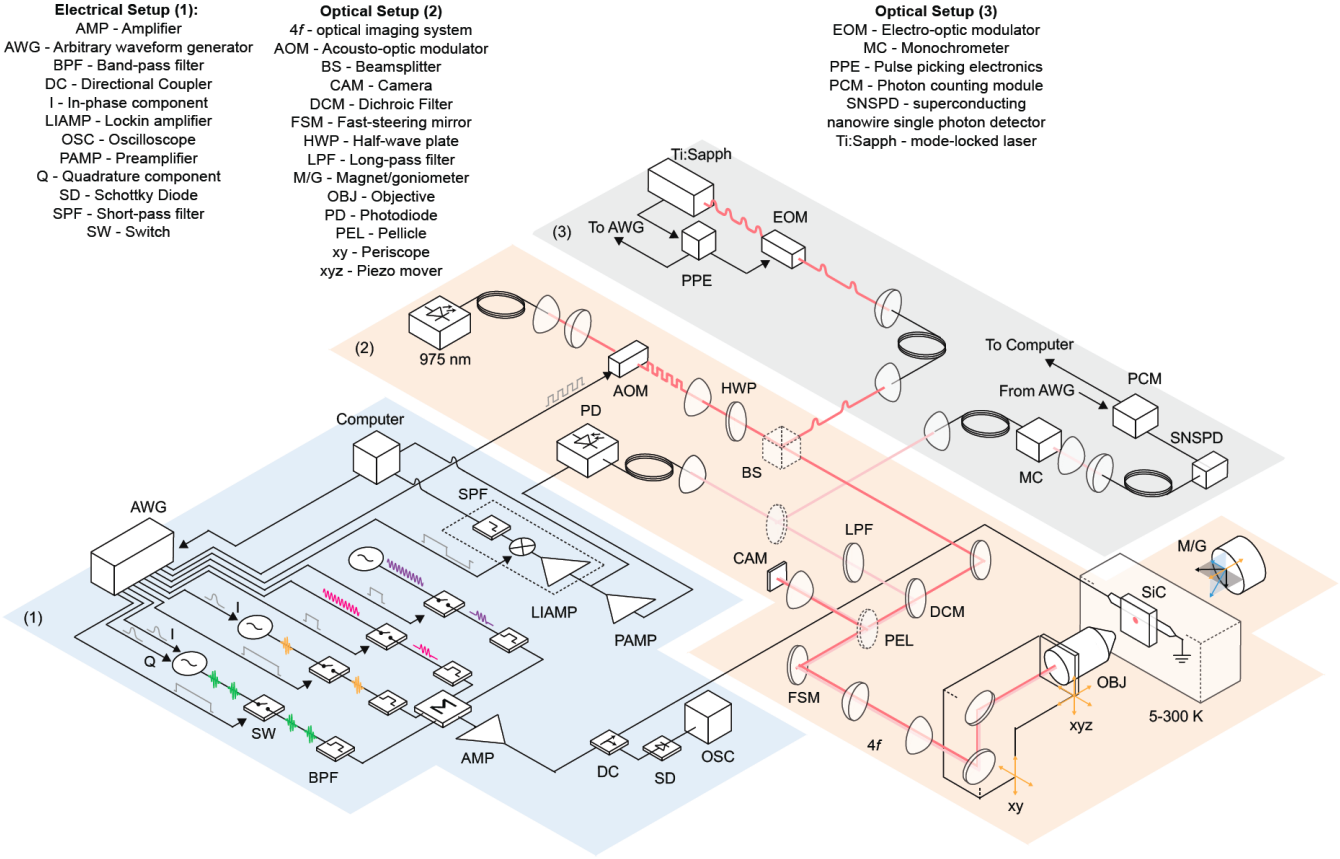

Fig. S4. Experimental Apparatus. General features of Electrical Setup (1) and Optical Setup (2) were used for our all of our measurements. Optical Setup (3) and the cryostat were integrated for the electron-spin-polarization measurement. The components are defined in the figure.

Table S1. The relative signal calculated for various registers.

R2 experiment	ESR (MHz)	Δ (MHz)	*Relative Signal*
R2	± 4.8	0	1
R22	$(\pm 9.6, 0)$	4.8	0.04
R21	$(\pm 1.5, \pm 11.1)$	6.3	0.03
R222	$(\pm 4.8, \pm 14.4)$	9.8	<0.01
R221	$(\pm 15.9, \pm 6.3, \pm 3.3)$	11.1	<0.01
R211	$(\pm 17.4, \pm 7.8, \pm 4.8)$	12.6	<0.01
R1 experiment	ESR (MHz)	Δ (MHz)	*Relative Signal*
R1	± 6.3	0	1
R11	$(\pm 12.6, 0)$	6.3	0.01
R12	$(\pm 1.5, \pm 11.1)$	4.8	0.10
R111	$(\pm 12.6, \pm 25.2)$	18.9	<0.01
R112	$(\pm 17.4, \pm 7.8, \pm 4.8)$	11.1	<0.01
R122	$(\pm 15.9, \pm 6.3, \pm 3.3)$	9.6	<0.01

Table S2. Quantum gate sequences used to measure the density matrix coherences. The quantum circuit representations of U_1 and U_2 are presented in Fig. 3D.

U_1	U_2	*Signal*
$R_0^n\left(\frac{\pi}{2}\right)R_0^{e1}(\pi)$	$R_{180}^n\left(\frac{\pi}{2}\right)R_0^{e1}(\pi)$	$2\Re(\rho_{14})(K_3-K_4)$
$R_0^n\left(\frac{\pi}{2}\right)R_0^{e2}(\pi)$	$R_{180}^n\left(\frac{\pi}{2}\right)R_0^{e2}(\pi)$	$-2\Re(\rho_{23})(K_3-K_4)$
$R_0^n\left(\frac{\pi}{2}\right)R_0^{e0}(\pi)$	$R_{180}^n\left(\frac{\pi}{2}\right)R_0^{e0}(\pi)$	$2\Im(\rho_{12})(K_3-K_4)$
$R_0^n\left(\frac{\pi}{2}\right)$	$R_{180}^n\left(\frac{\pi}{2}\right)$	$2\Im(\rho_{34})(K_3-K_4)$
$R_{90}^n\left(\frac{\pi}{2}\right)R_0^{e1}(\pi)$	$R_{270}^n\left(\frac{\pi}{2}\right)R_0^{e1}(\pi)$	$-2\Im(\rho_{14})(K_3-K_4)$
$R_{90}^n\left(\frac{\pi}{2}\right)R_0^{e2}(\pi)$	$R_{270}^n\left(\frac{\pi}{2}\right)R_0^{e2}(\pi)$	$-2\Im(\rho_{23})(K_3-K_4)$
$R_{90}^n\left(\frac{\pi}{2}\right)R_0^{e0}(\pi)$	$R_{270}^n\left(\frac{\pi}{2}\right)R_0^{e0}(\pi)$	$2\Re(\rho_{12})(K_3-K_4)$
$R_{90}^n\left(\frac{\pi}{2}\right)$	$R_{270}^n\left(\frac{\pi}{2}\right)$	$2\Re(\rho_{34})(K_3-K_4)$
$R_{90}^n\left(\frac{\pi}{2}\right)R_0^{e1}(\pi)R_0^n(\pi)$	$R_{270}^n\left(\frac{\pi}{2}\right)R_0^{e1}(\pi)R_0^n(\pi)$	$2\Re(\rho_{13})(K_3-K_4)$
$R_0^n\left(\frac{\pi}{2}\right)R_0^{e1}(\pi)R_0^n(\pi)$	$R_{180}^n\left(\frac{\pi}{2}\right)R_0^{e1}(\pi)R_x^n(\pi)$	$2\Im(\rho_{13})(K_3-K_4)$
$R_{90}^n\left(\frac{\pi}{2}\right)R_0^{e2}(\pi)R_0^n(\pi)$	$R_{270}^n\left(\frac{\pi}{2}\right)R_0^{e2}(\pi)R_0^n(\pi)$	$2\Re(\rho_{24})(K_3-K_4)$
$R_0^n\left(\frac{\pi}{2}\right)R_0^{e2}(\pi)R_0^n(\pi)$	$R_{180}^n\left(\frac{\pi}{2}\right)R_0^{e2}(\pi)R_0^n(\pi)$	$-2\Im(\rho_{24})(K_3-K_4)$

Table S3. Quantum gate sequences used to measure the density matrix populations. Note that only three of these four equations are linearly independent. It therefore suffices to make only three of these measurements. For the reconstruction presented in the main text, we use the first three sequences. The quantum circuit representations of U_1 and U_2 are presented in Fig. 3C.

U_1	U_2	*Signal*
$R_0^n(\pi)R_0^{e1}(\pi)$	$R_0^{e1}(\pi)$	$-(K_3-K_4)(\rho_{11}-\rho_{44})$
$R_0^n(\pi)R_0^{e2}(\pi)$	$R_0^{e2}(\pi)$	$-(K_3-K_4)(\rho_{33}-\rho_{22})$
$R_0^n(\pi)R_0^{e0}(\pi)$	$R_0^{e0}(\pi)$	$-(K_3-K_4)(\rho_{11}-\rho_{22})$
$R_0^n(\pi)$	$-$	$-(K_3-K_4)(\rho_{33}-\rho_{44})$

Table S4. Consolidated initialization and entanglement data. The left-most column shows the ideal states. The electron spin polarization P_e is defined in Eq. S10 and the nuclear spin polarization is defined as $\boldsymbol{P_n} = \frac{\boldsymbol{\rho_{11}-\rho_{22}}}{\boldsymbol{\rho_{11}+\rho_{22}}}$. The error bars represent the 95% confidence intervals.

R2	P_n	P_e	F	*PPT test*
$\|0,\uparrow\rangle$	$99^{+1}_{-3}\%$	$93^{+7}_{-11}\%$	$0.95^{+0.05}_{-0.07}$	-0.01±0.02
$\|\Phi^+\rangle$	-	-	0.78±0.07	-0.31±0.06
$\|\Phi^-\rangle$	-	-	0.79±0.07	-0.31±0.07
$\|\Psi^+\rangle$	-	-	0.88±0.07	-0.40±0.06
$\|\Psi^-\rangle$	-	-	0.85±0.07	-0.37±0.06
R1	P_n	P_e	F	*PPT test*
$\|0,\uparrow\rangle$	91±8%	$89^{+11}_{-12}\%$	0.89±0.08	-0.004±0.011
$\|\Phi^+\rangle$	-	-	0.76±0.07	-0.29±0.06
$\|\Phi^-\rangle$	-	-	0.73±0.07	-0.25±0.05
$\|\Psi^+\rangle$	-	-	0.77±0.07	-0.30±0.06
$\|\Psi^-\rangle$	-	-	0.78±0.07	-0.32±0.06